Propagation Modeling for Radio Frequency Tomography in Wireless Networks

Benjamin R. Hamilton, *Member, IEEE,* Xiaoli Ma, *Senior Member, IEEE,* Robert J. Baxley, *Senior Member, IEEE,*, and Stephen M. Matechik, *Member, IEEE,*

Abstract—Non-cooperative localization is an important class of applications with the goal of detecting and tracking objects without their explicit participation. Recognizing that these objects will attenuate any radio signals that pass through them, recent works have proposed using the received signal strength (RSS) measurements from networks of portable wireless devices to detect, localize, and track objects through radio frequency (RF) tomography. Because the effects of these objects on radio signals can be relatively small, accurate radio propagation models are essential to the accuracy and reliability of these methods. Despite their critical importance, only limited work has been done to develop and test such models.

In this paper, we describe the RF tomography problem in detail, comparing both existing and novel shadowing models analytically. We design an RF tomography testbed and describe the techniques used to conduct field test measurements. We present the experimental results from our RF tomography testbed comparing several different shadowing models. Further, we present the results of applying the different shadowing models to RSS measurements obtained in a field test and evaluate how well each model approximates the radio propagation experienced during our test.

I. INTRODUCTION

The development of the capability to field large, self-organizing ad hoc networks promise a revolution in communications with increased flexibility and reliability and reduced deployment and maintenance costs. When these networks are combined with new miniaturized sensing technologies, they can be used to collect unparalleled amounts of sensing data and show enormous promise in applications ranging from intrusion detection to environmental monitoring [1].

In dense networks with large numbers of wireless devices, the received signal strength (RSS) measurements between all the wireless nodes in the network contain a significant amount of information about the environment the network is operating in. As radio transmissions pass through the

environment, the signal is attenuated by the objects it passes through, causing shadowing. Several recent works [2]–[4] have combined techniques from tomographic imaging, such as filtered backprojection [5], with propagation and shadowing models to use the deviations in RSS measurements due to this shadowing for through-wall detection and tracking of both static and moving objects. Such a capability has compelling applications ranging from surveillance to locating survivors in rescue operations. It can also be used to track movement and location of people or objects through "device-free passive localization" [6].

A key problem in using shadowing measurements for detection and tracking is determining an efficient and accurate method for extracting information about the structure of the network environment from the measurements. Although a few techniques to extract environmental information from received radio signals have been used for imaging in geophysics for some time [7], [8], these methods are designed for complicated situations where scattering and reflective effects are significant. To compensate for these effects they require the phase information from the received signal and reconstruct an image by simultaneously solving the discretized wave equations for each signal measurement. While the these techniques have relatively high accuracy, the extremely large computational costs make any sort of real-time implementation impractical. We instead focus on simpler systems where the scattering and reflective effects are less significant so that simpler approximations for the wireless propagation based on shadowing can be used.

While an enormous amount of research has focused on characterizing the effect of shadowing on radio frequency (RF) propagation, few models relate the shadowing experienced by a signal to attenuation at specific points in space, which limits their utility for RF tomography. Traditional shadowing models such as the log-normal shadowing model [9] assume shadowing for each link is independent. The information about shadowing objects in the network however, is encoded in the correlation between shadowing in links in the network. Similarly, while other shadowing models [10], [11]) have described the shadowing correlation when one of the nodes in the link is mobile, this model does not provide a relationship between the path taken by the radio transmission through space and the shadowing experienced.

The "Joint Path Loss Model" described in [12] was able to provide an approximate model for the relationship between shadowing and the path travelled by the radio transmission. Under this model the shadowing component of the wireless links η is related to the line integral from source to destination

of an underlying spatial loss field $g(s)$ which represents the additional attenuation due to shadowing at each point s in space. This model was later used by the Network Shadowing (NeSh) model [13] and a noninvasive mapping algorithm [14].

Some other recent works [2], [3], [15] have relied on the observation of significant time variation in the RSS measurements from links that are obstructed by an object and use the variance in the RSS measurements for imaging. While the earlier works [2], [3] use an approximation of the NeSh model where the line integral is replaced with with an integral of an ellipse with the transmitter and receiver as foci, more recent work [15] has found that Cassini ovals are more representative of the measured RSS variance.

While a couple of models have been presented in the literature, there has been insufficient comparison or experimental verification of these shadowing models in more complicated shadowing environments. While a few recent works [15], [16] have focused on model verification, these experiments relied on the low quality transceivers present on wireless sensor motes and only considered the effects of a single small object. This limits their ability to separate the error sources and limitations of the RF platform from limitations in the accuracy of the shadowing models. Additionally, the low complexity shadowing environments explored in these works do not fully exercise the shadowing model.

This work is aimed at providing such experimental verification using higher quality measurements. To that end, the primary contributions of this work are:

- Describe and analyze existing shadowing models
- Introduce a new shadowing model, the inverse area elliptical model
- Present the design and construction of our RF tomography testbed
- Evaluate and compare how consistent each of the shadowing models are with the measurements collected from our field test

II. System Model

Consider a additive white Gaussian noise (AWGN) channel between two nodes. The transmitted signal x is received as:

$$y = hx + u, \qquad (1)$$

where h is the wireless channel gain and u is additive white Gaussian noise [17]. Note that while this model assumes a single-path propagation model, it can be extended to multipath channels if only the first arriving path is considered, and the other delayed paths treated as noise. The channel gain h can be decomposed into four primary components: the free space path loss, attenuation due to shadowing, receiver gains S (such as antenna gain and cabling losses), and transmitter gains T. For the channel between transmitter n and receiver m, the channel $h_{n,m}$ can be written as

$$h_{n,m} = \sqrt{T_n S_m} \quad \underbrace{d_{n,m}^{-\alpha/2}}_{\text{free space path loss}} \quad \underbrace{10^{\frac{\eta}{20}}}_{\text{attenuation due to shadowing}}, \qquad (2)$$

where $d_{n,m}$ is the distance between transmitter n and receiver m, α is the path loss exponent (nominally between 2 and 4), and η is the shadowing component.

The shadowing component is some function of the spatial loss field (SLF) $g(s)$, which has a domain of every point in space s. For modeling purposes, this SLF has been assumed to have a Gaussian distribution, with a covariance between points separated by a distance $d_{n,m}$:

$$R_g(d_{n,m}) = \frac{\sigma_\eta^2}{\kappa} e^{-\frac{d_{n,m}}{\kappa}}, \qquad (3)$$

where σ_η^2 is the shadowing covariance and κ is a parameter controlling how fast the correlation falls off with distance [12].

We assume that the RSS measurements are proportional to the channel estimate. In practical systems the proportionality constant can be determined and eliminated, so without loss of generality we can model the RSS measurement $z_{n,m}$ from node n to node m with the channel estimate $h_{n,m}$ from (2). Assuming the distance, path loss exponent, and receiver/transmitter gains are known, the shadowing component can then be estimated as

$$\hat{\eta}_{n,m} = 10 \log_{10} \frac{h_{n,m}^2}{T_n S_m d_{n,m}^{-\alpha}}. \qquad (4)$$

Due to the NLOS effects, an accurate calculation of the shadowing component from the spatial loss field in the network area is nonlinear. Such nonlinear tomographic projection models are generally difficult to deal with in practice. Thus, we consider linear tomographic projection models. More specifically, we examine shadowing models such that the shadowing on the link between nodes at positions s_n and s_m is found as the spatial integral of the spatial loss field over the network area weighted by some function $b(s_n, s_m, s)$:

$$\eta_{n,m} = \int g(s) b(s_n, s_m, s) \quad ds. \qquad (5)$$

For practical purposes, the spatial loss field is always discretized so that instead of representing how every point in space contributes to the total path loss, it aggregates the points into pixels (or voxels) and describes how much each pixel contributes to the total path loss. In the discretized version of the model, the field is replaced by a column vector g. The exact relationship between the continuous field $g(s)$ and the discrete approximation g depends on the model. The line integral in (5) is then replaced by a vector product such that:

$$\eta_{n,m} = b_{n,m} g, \qquad (6)$$

where $b_{n,m}$ is the discrete tomographic projection row vector with elements corresponding to each discrete (x,y) pixel in the field g.

For example, consider Figure 1. In Figure 1(a) we have several transceivers (red circles) which take path loss measurements across each of the (black) paths to the other transceivers. Since the measurement (in dB) between any given pair of transceivers n and m are linear functions of the spatial loss field such that $\eta_{n,m} = b_{n,m} g$, we can rewrite this in matrix form as

$$\eta = Bg, \qquad (7)$$

where B is a matrix containing the row vectors $b_{n,m}$ for all transceivers pairs (n, m) and the vector η contains the corresponding measurements, $\eta_{n,m}$. For instance, if there are
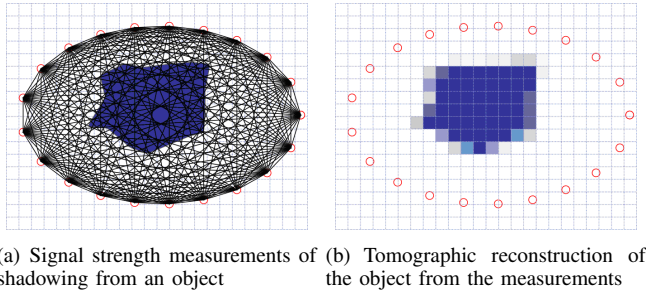
(a) Signal strength measurements of shadowing from an object
(b) Tomographic reconstruction of the object from the measurements

Fig. 1. Shadowing example

(a) NeSh Model

(b) Normalized Ellipse Model

(c) Inverse Area Elliptical Model

Fig. 2. Example weight vectors for the three tomographic models

three transceivers in the network, l, n and m, the three link measurements can be expressed by the matrix equation,

$$\underbrace{\begin{bmatrix} \eta_{l,m} \\ \eta_{l,n} \\ \eta_{m,n} \end{bmatrix}}_{\boldsymbol{\eta}} = \underbrace{\begin{bmatrix} \boldsymbol{b}_{l,m} \\ \boldsymbol{b}_{l,n} \\ \boldsymbol{b}_{m,n} \end{bmatrix}}_{\boldsymbol{B}} \boldsymbol{g}. \tag{8}$$

Then the spatial loss field can be estimated as

$$\hat{\boldsymbol{g}} = \boldsymbol{B}^{-1}\boldsymbol{\eta}. \tag{9}$$

A visual example of the tomographic reconstruction corresponding to the measurements in Figure 1(a) can be found in Figure 1(b).

In most cases, however the inversion in (9) is not possible since $\boldsymbol{B}$ is under-determined; i.e. there are many more SLF pixels than there are measurements. To compensate for this, regularization techniques such as Tikhonov regularization are applied. These techniques use some prior information of the form of the solution such as its expected covariance to stabilize the reconstruction. In addition to compensating for the poor condition of the projection matrix $\boldsymbol{B}$, regularization also can compensate for inaccuracies in the projection model by forcing the solution to resemble the prior information. While the ability of regularization to compensate for modeling error can be helpful, this effect needs to be considered when evaluating and comparing the accuracy of different models. We will revisit this issue in Section IV-B when we compare the different propagation models. When Tikhonov regularization is applied, the reconstructed image can be found as

$$\hat{\boldsymbol{g}} = \left(\boldsymbol{B}^H\boldsymbol{B} + \omega \boldsymbol{C}_g^{-1}\right)^{-1}\boldsymbol{B}^H\boldsymbol{\eta}, \tag{10}$$

where ω is the regularization weight and $\boldsymbol{C}_g$ is the expected covariance matrix of the spatial loss field (i.e. $\boldsymbol{C}_g = E[\boldsymbol{gg}^T] - E[\boldsymbol{g}]E[\boldsymbol{g}]^T$) containing entries for the covariance of each pair of pixels n and m which are distance a $d_{n,m}$ apart, calculated as in (3).

In this work we consider three distinct projection models, each with their own method of calculating the projection weight matrix $\boldsymbol{B}$. A visual comparison of the weight vectors for the three different shadowing models we are considering is shown in Figure 2, and they are each described in more detail below.

A. NeSh Model

In the NeSh model, the path loss from shadowing is assumed to be proportional to a line integral across the spatial loss field.
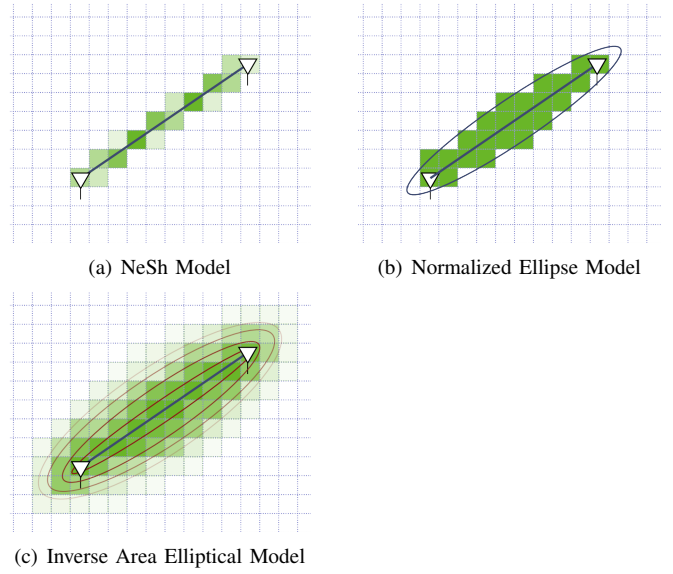
This is the most common model used in CT, and a modification for RF Tomography was introduced as the Network Shadowing (NeSh) model [12], [13]. The NeSh model differs from traditional tomographic line integral model in that the weights are multiplied by the square root of the path length. This means the tomographic projection is

$$b(\boldsymbol{s}_n, \boldsymbol{s}_m, \boldsymbol{s}) = \frac{1}{\sqrt{d_{n,m}}} \int_{\boldsymbol{s}_n}^{\boldsymbol{s}_m} \delta(|\boldsymbol{s} - \tilde{\boldsymbol{s}}|) \quad d\tilde{\boldsymbol{s}}, \tag{11}$$

where $\delta(x)$ is the Dirac delta function. With this model, the shadowing component simplifies as

$$\eta_{n,m} = \frac{1}{\sqrt{d_{n,m}}} \int_{\boldsymbol{s}_n}^{\boldsymbol{s}_m} g(\boldsymbol{s}) \quad d\boldsymbol{s}. \tag{12}$$

This modification was made so that the model matches the larger scale shadowing statistical models. It was necessary because this model does not consider the effects of diffraction at all. This modification only changes the large scale statistics. This means that, even with this modification, diffraction will cause significant artifacts in the reconstruction.

As mentioned previously, a discretized tomographic projection vector $\boldsymbol{b}$ is usually used instead of the continuous tomographic projection function $b(\boldsymbol{s}_n, \boldsymbol{s}_m, \boldsymbol{s})$ listed above. The tomographic projection vector $\boldsymbol{b}_{n,m}$ for this model is a vector of weights with entries equal to length of the path that falls within the corresponding pixel, divided by the square root of the path length. A visual example of the weights from this model is shown in Figure 2(a).

B. Normalized Ellipse Model

In the Normalized Ellipse model, the tomographic projection consists of a selection function based on an ellipse that has the transmitter and receiver as foci and some semi-minor axis length λ. The selection function has a value of $\frac{1}{d_{n,m}}$ inside the ellipse, and 0 elsewhere. This model has also been previously

used for RF Tomography [2], [3], [18]. Mathematically we can represent this model as

$$b(\boldsymbol{s}_n, \boldsymbol{s}_m, \boldsymbol{s}) = \begin{cases} \frac{1}{\sqrt{d_{n,m}}} & \frac{p_x(\boldsymbol{s}_n, \boldsymbol{s}_m, \boldsymbol{s})^2}{d_{n,m}^2 + \lambda^2} + \frac{p_y(\boldsymbol{s}_n, \boldsymbol{s}_m, \boldsymbol{s})^2}{\lambda^2} < 1 \\ 0 & \text{else} \end{cases},$$

(13)

where $p_x(\boldsymbol{s}_n, \boldsymbol{s}_m, \boldsymbol{s})$ and $p_y(\boldsymbol{s}_n, \boldsymbol{s}_m, \boldsymbol{s})$ are projection functions that project the point $\boldsymbol{s}$ onto an axis aligned parallel to the line from $\boldsymbol{s}_n$ and $\boldsymbol{s}_m$, and centered between $\boldsymbol{s}_n$ and $\boldsymbol{s}_m$.

Based on geometry, we can define the projections functions $p_x(\boldsymbol{s}_n, \boldsymbol{s}_m, \boldsymbol{s})$ and $p_y(\boldsymbol{s}_n, \boldsymbol{s}_m, \boldsymbol{s})$ as

$$p_x(\boldsymbol{s}_n, \boldsymbol{s}_m, \boldsymbol{s}) = \psi_x(s_x - c_x) + \psi_y(s_y - c_y) \quad (14)$$

$$p_y(\boldsymbol{s}_n, \boldsymbol{s}_m, \boldsymbol{s}) = -\psi_y(s_x - c_x) + \psi_x(s_y - c_y), \quad (15)$$

where the projection vector $\boldsymbol{\psi}$

$$\boldsymbol{\psi} = \begin{bmatrix} \psi_x & \psi_y \end{bmatrix}^T = \frac{\boldsymbol{s}_n - \boldsymbol{s}_m}{||\boldsymbol{s}_n - \boldsymbol{s}_m||} \quad (16)$$

and $\boldsymbol{c}$ is the position of the center of the ellipse

$$\boldsymbol{c} = \frac{\boldsymbol{s}_n + \boldsymbol{s}_m}{2}. \quad (17)$$

There is some physical justification for using an ellipse, as the well-known Fresnel zone has an ellipsoidal shape. A problem with this model is that there is not a good physical basis for determining the parameter λ. Current methods using this model find the parameters of the ellipse through trial and error. Additionally the decision to set the weights of all of the pixels equally also has no physical justification.

The discrete tomographic projection vector $\boldsymbol{b}_{n,m}$ corresponding to this model has weights for each pixel are equal to the continuous projection function $b(\boldsymbol{s}_n, \boldsymbol{s}_m, \boldsymbol{s})$, evaluated at the center of the pixel. For an NxN field $\boldsymbol{g}$ with pixels centered at positions $\boldsymbol{s}_{p_{x,y}}$, we can write

$$\begin{aligned} \boldsymbol{b}_{n,m} = \big[& b(\boldsymbol{s}_n, \boldsymbol{s}_m, \boldsymbol{s}_{p_{0,0}}) , \ b(\boldsymbol{s}_n, \boldsymbol{s}_m, \boldsymbol{s}_{p_{1,0}}), \ \cdots, \\ & b(\boldsymbol{s}_n, \boldsymbol{s}_m, \boldsymbol{s}_{p_{N-1,0}}), \ b(\boldsymbol{s}_n, \boldsymbol{s}_m, \boldsymbol{s}_{p_{0,1}}), \ b(\boldsymbol{s}_n, \boldsymbol{s}_m, \boldsymbol{s}_{p_{1,1}}), \\ & \cdots, \ b(\boldsymbol{s}_n, \boldsymbol{s}_m, \boldsymbol{s}_{p_{N-1,N-1}}) \big] \end{aligned} \quad (18)$$

A visual example of this model is shown in Figure 2(b).

C. Inverse Area Elliptical Model

We introduce the a new shadowing model, the inverse area elliptical model. In this model, the tomographic weighting function $b(\boldsymbol{s}_n, \boldsymbol{s}_m, \boldsymbol{s})$ is equal to the inverse of the area of the smallest ellipse containing $\boldsymbol{s}$ that has the transmitter and receiver as foci. As mentioned previously, there is some physical justification for using an ellipse in the projection model, as the well-known Fresnel zone has an ellipsoidal shape. While the Normalized Ellipse model assumed that all the points inside the ellipse have equal weight, our inverse area elliptical model recognizes that some parts of the ellipse have a greater contribution than others. Since the portion of the signal travelling near the edge of the ellipse travels a longer distance than the portions travelling nearer to line of sight, they will be weaker, and contribute less to the total RSS. In the inverse area elliptical model, this is reflected by weighting

points farther from the line of sight (contained in ellipses with larger areas) less than points closer to the line of sight.

Mathematically we can represent this model as

$$b(\boldsymbol{s}_n, \boldsymbol{s}_m, \boldsymbol{s}) = \frac{1}{\pi \tilde{\mu}_{n,m} \sqrt{d_{n,m}^2 + \tilde{\mu}_{n,m}^2}}, \quad (19)$$

where the parameter $\tilde{\mu}_{n,m}$ is the length of the semi-minor axis of the smallest ellipse containing the point $\boldsymbol{s}$. More formally,

$$\tilde{\mu}_{n,m} = \arg\min_{\mu} \left| \frac{p_x(\boldsymbol{s}_n, \boldsymbol{s}_m, \boldsymbol{s})^2}{d_{n,m}^2 + \mu^2} + \frac{p_y(\boldsymbol{s}_n, \boldsymbol{s}_m, \boldsymbol{s})^2}{\mu^2} - 1 \right|. \quad (20)$$

We bound the weights by setting minimum and maximum semi-minor axis lengths $\mu_{\min}$ and $\mu_{\max}$. The weight for points within the smallest ellipse is equal to the inverse of the area of the smallest ellipse. The weight for points outside the largest ellipse are set to 0. We set $\mu_{\min}$ to 0 and $\mu_{\max}$ to the length of the semi-minor axis of the first Fresnel ellipse. This selection of $\mu_{\max}$ provides a wide enough area for the projection so that the contributions from further areas would be negligible. This model is more complicated than the Normalized Ellipse model, but should better capture the relative strengths of diffracted paths.

For the discrete tomographic projection vector based on this model, the weights for each pixel are equal to the continuous weight $b(\boldsymbol{s}_n, \boldsymbol{s}_m, \boldsymbol{s})$, evaluated at the center of the pixel. This is analogous to the conversion described in Eq. (18) for the Normalized Ellipse model. A visual example of this model is shown in Figure 2(c).

III. EXPERIMENT DESIGN

We designed our RF tomography testbed to emulate the conditions that would be expected in a practical application of RF tomography. The testbed consisted of two primary components, an artificial structure, and the channel measurement equipment. The key difference between this testbed and the testing done in previous works [2], [3] is that we are trying to determine the accuracy of the shadowing models.

A. Artificial Structure

The artificial structure was specifically designed to create a complex radio propagation environment. It was constructed out of plywood, sheetrock, concrete board and cinder block. In order to provide a more complicated shadowing environment the structure was designed with interior walls and a cinder block pillar in addition to the exterior walls. This provides a more complicated environment which should challenge the shadowing models we are testing. Each wall was composed of 3 modular 8 ft. high by 4 ft. wide panels supported by a 2x4 wood stud assembly. We constructed a total of 13 panels with the following breakdown:

- 3 3/8 in. plywood panels (exterior) with R11 insulation and sheetrock (interior)
- 3 1/2 in. OSB panels (exterior)
- 3 concrete board panels (exterior)
- 2 1/2 in. plywood panels (exterior)
- 1 1/2 in. plywood panel (interior)

- 1 sheetrock panel (interior)
- 1 column of cinder blocks

A diagram of the completed structure is shown in Figure 3.

B. Channel Measurement Equipment

Unlike previous works, we needed to make more accurate channel measurements so that we could separate errors in the tomographic reconstruction due to modeling error from those due to noise. Additionally, we needed to take significantly more channel measurements to detect the modeling error. In order to achieve both the accuracy and collection efficiency required, the channel measurements were collected using 10 Agilent E443x programmable signal generators as the transmitters and 10 Ettus USRP2 [19] software defined radios as the receivers. The flexibility of these devices allowed us to completely control the transmission and reception processes.

The software radios serving as the receivers were each connected over gigabit Ethernet to a laptop running Linux. The laptop was responsible for controlling the USRP2 radios and temporarily storing the raw samples of the received signal as it was being collected. The laptops in turn were controlled through a separate Ethernet network connecting them to the control computer. The control computer was connected to each laptop through Secure SHell (SSH) so that the control computer could trigger data collection and download the collected samples. This level of automation was necessary in order to collect a large number channel measurements in a limited period of time.

The outputs of the transmitters and inputs of the receivers were connected to 12dB omni-directional antennas through 20 ft. long RF cables. These antennas were mounted on tripods which could be moved to measure the propagation characteristics between different parts of the network. The transmitters and receivers were also connected to rubidium atomic clocks as frequency references, to limit the error due to frequency offsets.

C. Signal Design and Measurement

The signal generators serving as transmitters were programmed with channel sounding sequences designed for multi-user multiple input multiple output (MIMO) communication systems [20]. These sequences consist of a set of polyphase chirp waveforms which are all orthogonal and robust to differences in transmitter timing. In our testbed, the nth transmitter was programmed with the sequence

$$s_n[t] = e^{j\pi 2^n \frac{t(t+1)}{K}}, \quad (21)$$

for $n \in \{1, 2, \ldots, 10\}$ and $t \in \{0, 1, \ldots, K-1\}$. Using orthogonal waveforms allowed us to use the 10 transmitters and 10 receivers to simultaneously estimate 100 channels. Since these sequences are robust to differences in timing, we did not need to synchronize the transmission of these sequences. This allowed us to configure the transmitters to transmit continuously throughout the entire field test without needing a complex triggering system to synchronize the transmitters and receivers. Further, since we used very long
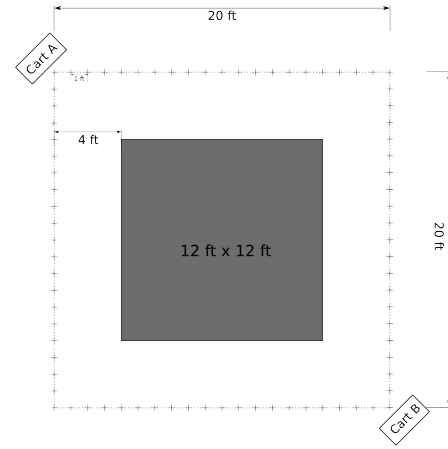

Fig. 4. Collection Layout

transmit sequences ($K = 2^{14}$ samples), we had an extremely high processing gain at the receiver, allowing us to obtain very high accuracy channel estimates. The channel measurement for the link from transmitter n to receiver m were then extracted from the received sequence $r_m[t]$ using a matched filter

$$\hat{h}_{n,m}[t] = \sum_{k=0}^{K} s_n[t-k] r_m[k], \quad (22)$$

where the indices are taken modulus K. The maximum of the magnitude of the channel estimate ($\arg\max_t \hat{h}_{n,m}[t]$) was then taken as the RSS estimate.

D. Data Collection

The equipment was divided onto two carts: Cart A, which hosted 6 transmitters and 6 receivers, and Cart B, which hosted 4 transmitters and 4 receivers. Each cart was connected to an independent EU3000 Honda generator to provide power. The control computer was co-located with Cart B and connected to the control network. The transmitters and receivers were configured so that channel measurements were taken at 2.425GHz with 5MHz bandwidth at a sampling rate of 5 million samples/sec. Note that this 5MHz of bandwidth is insufficient to resolve multipath within the structure, so it will be treated as noise. For the purposes of calibration, all measurements were taken twice, once with the artificial structure present and again with it completely removed.

We measured the channel estimate for links between all combinations of positions on the perimeter of a 21x21 grid, a total of 2400 unique links. The grid spacing was 1 ft. , and the perimeter was around 4 ft. from the structure. A diagram of the collection configuration is shown in Figure 4, where the solid 12 ft. x 12 ft. block represents the artificial structure.

Since we were only using 10 receivers and 10 transmitters, the measurements were collected in a series of 24 steps. Between collection steps, either the receiver antennas or the transmitter antennas were moved to sound a different set of links. The collection process can be divided into major movements, where one set of the antennas needed to be shifted from one edge of the grid to another and minor
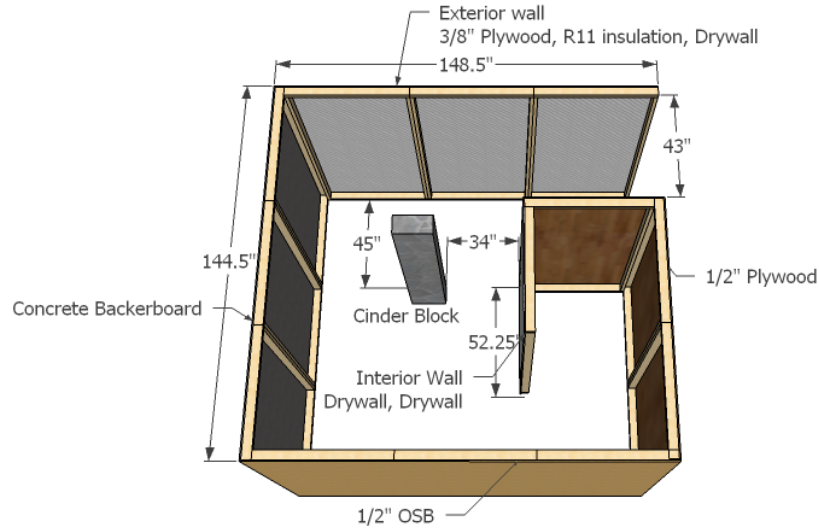
Fig. 3. Diagram of shadowing structure

(a) Step 1

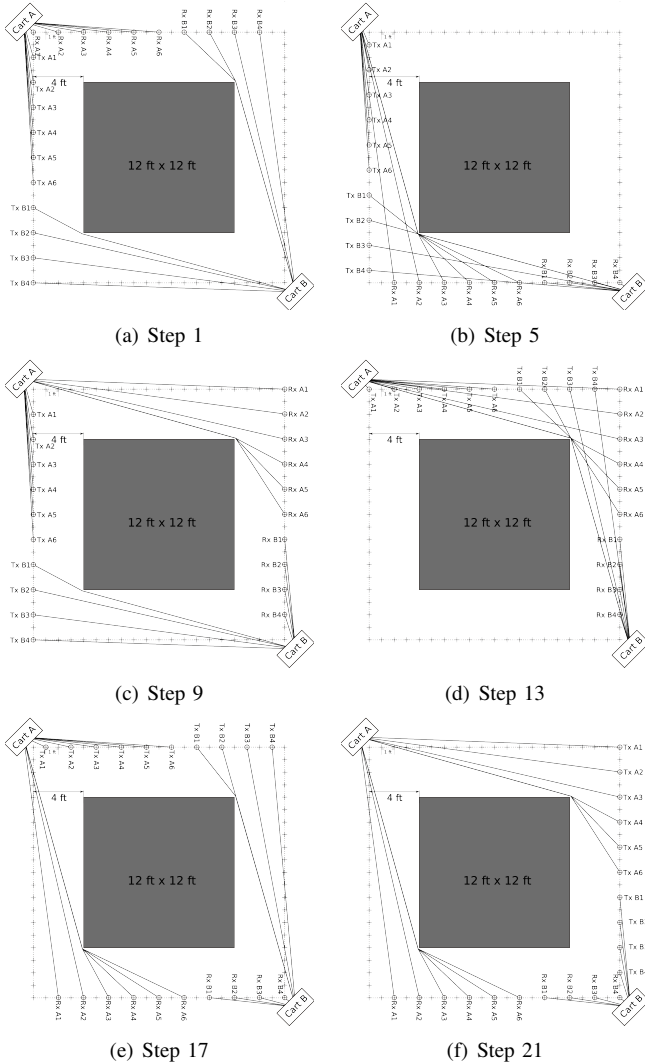(b) Step 5

(c) Step 9

(d) Step 13

(e) Step 17

(f) Step 21

Fig. 5. Measurement Steps

movements where the antennas were simply shifted 1 ft. along the perimeter while staying on the same side of the grid. Each major movement was followed by three minor movements and the minor movements followed the sequence of moving the receiver antennas (clockwise), then the transmitter antennas (alternating after each major movement, starting with clockwise), and then the receiver antennas (counter clockwise). Diagrams of the transmitter and receiver antenna positions after each major movement are shown in Figure 5, where the circles show antenna positions, and the lines show how the cable was routed from the cart to the antenna. The data collected from all of these steps was composited into a single large data set which was then used for the reconstruction.

IV. ANALYSIS AND RESULTS

We obtained the measurements from the testbed described in Section III. These results were then used to estimate system parameters, which were then combined with reconstruction parameters to perform the reconstructions used in the subsequent analysis.

A. Calibration and RF environment analysis

Before the reconstruction can be calculated there are several aspects of the testbed that need to be characterized. Of primary importance are the transmitter and receiver gains T and S for each transmitter and receiver, but additionally the path loss exponent α also needs to be estimated. We jointly estimated these parameters from the data collected in the absence of the structure using least-squares (LS). Converting (2) into its decibel domain equivalent (i.e., $h_{n,m}^{dB} = 10 \log_{10} h_{n,m}$) and setting the shadowing component to 0, we have:

$$h_{n,m}^{\mathrm{dB}} = T_n^{\mathrm{dB}} + S_m^{\mathrm{dB}} - 10\alpha \log_{10} d_{m,n}. \qquad (23)$$

Combining the channel measurements for every measured link into a matrix equation (in a manner similar to (8)), we have

$$\boldsymbol{h}^{\mathrm{dB}} = \begin{bmatrix} \boldsymbol{\Omega} & -10 \log_{10} \boldsymbol{d} \end{bmatrix} \begin{bmatrix} \boldsymbol{T}^{\mathrm{dB}} \\ \boldsymbol{S}^{\mathrm{dB}} \\ \alpha \end{bmatrix}, \qquad (24)$$

where $\mathbf{\Omega}$ is a selection matrix which selects the elements from the $\mathbf{T}$ and $\mathbf{S}$ vectors to be used for each link, and $\mathbf{d}$ is the corresponding vector of link distances. This equation is underdetermined because a constant amount of gain can be shifted from all of the transmitter gains to the receiver gains and still satisfy the equation. Without loss of generality, we arbitrarily set $T_0^{dB} = 0$ and then solved the equation to find the other calibration parameters. While transmitter and receiver gains are testbed-dependent and are thus omitted, we found he path loss exponent for the environment we were testing to be approximately 2.

B. Reconstruction Parameter Selection

The reconstructed image quality is dependent on several parameters such as the resolution and number of pixels in the reconstructed image and the parameters for any regularization applied in the reconstruction. Several constraints limit image quality in terms of resolution, signal to noise ratio (SNR), and number and severity of imaging artifacts. Additionally there is a fundamental physical limit on the resolution in noncoherent imaging called the diffraction limit [21], that restricts the minimum distinguishable feature size to at least half of a wavelength of the frequency used for imaging. The primary limitation in our system, however, is the invertibility or stability of the projection matrix. As the resolution, or number of pixels in the desired reconstruction, increases the stability of the projection matrix decreases. This reduction in stability decreases the SNR and increases in the number and severity of imaging artifacts. While regularization can be used to increase the SNR and reduce the severity of imaging artifacts, regularization does so by forcing the reconstructed image to match a model of the expected reconstruction. In our case, we expect the SLF of the reconstruction to have spatial covariance between points separated by a distance $d_{n,m}$ by (3). Applying this model using Tikhonov regularization and the pixel covariance matrix $\mathbf{C}_g$ to the reconstruction results in a significant amount of smoothing in the image because pixels that are near eachother are forced to be be correlated. This smoothing causes the effective resolution in terms of minimum distinguishable feature size of the image to be smaller than the reconstructed image resolution in pixels.

The regularization parameters play a strong role in determining how well noise and artifacts are suppressed in the reconstruction. As mentioned previously, the two regularization parameters used to model the reconstructed SLF are σ_η^2, the shadowing covariance, and κ, a parameter controlling how fast the correlation falls off with distance. If κ is set too small, the correlation between pixels will fall off too quickly with distance and regularization will not significantly improve the stability of the reconstruction. In contrast, when κ is too large, the regularization will remove the details of small features. Since the feature size of the image we were interested in was around 3-4 in. (the thickness of the walls), we chose a value of $\kappa = 1$ in. to allow the spatial loss field to vary sufficiently over this interval. The other regularization parameters are the shadowing covariance σ_η^2 and the regularization weight ω. Combining (10) with the pixel covariance matrix $\mathbf{C}_g$, we find the ratio of ω to σ_η^2 effectively controls the amount of correlation between neighboring pixels. Small values of $\frac{\omega}{\sigma_\eta^2}$ allow adjacent pixels to be significantly different, reducing the effects of regularization. In contrast, large values of $\frac{\omega}{\sigma_\eta^2}$ constrain neighboring pixels to have nearly the same value, increasing the effect regularization has on the reconstruction and causing a significant amount of smoothing.

While numerous combinations of parameters were evaluated, we selected three scenarios which show a representative sample of the reconstruction performance of each of the shadowing models under different parameters:

- *No Regularization*: We employ a pure least-squared reconstruction to generate a 24x24 pixel image of the structure. This scenario is important because it shows how well the different models can reconstruct the image without the aid of any prior information about the SLF. Due to the limited stability of the projection matrix, a 24x24 pixel size resolution was chosen as it provided a good balance between the imaging resolution and the amount of noise and imaging artifacts.
- *Regularized (low smoothing)*: We set the parameters $\frac{\omega}{\sigma_\eta^2} = 25$ and $\kappa = 1$ in. to generate a 60x60 pixel reconstructed image. With these parameters, the regularization had only a small smoothing effect on the reconstructed image. This scenario was chosen to show how well the models perform when the regularization parameters are tuned for a relatively high resolution reconstruction. The relatively low shadowing covariance in the regularization provides noise and artifact suppression without causing significant smoothing.
- *Regularized (high smoothing)*: We set the parameters $\frac{\omega}{\sigma_\eta^2} = 278$ and $\kappa = 1$ in. to generate a 30x30 pixel reconstructed image. These regularization parameters caused the resulting image to have significant smoothing effects from the regularization. The settings for this scenario were chosen to provide good noise and artifact suppresion, with less concern with achieving high resolution.

C. Tomographic Reconstruction

We used the calibration parameters to calculate the measured shadowing across each link. These shadowing measurements were then used to performed tomographic reconstructions for each of the models described in Section II for each of the scenarios described. For the Normalized Ellipse model, the parameter λ was set to 1.2 in. as in [2].

Before directly examining the reconstructed images, we first consider how consistent each of the shadowing models is with the measured shadowing from the experiment. To quantify this consistency, we are going to examine the sum of square residuals (SSR) from the reconstruction. For the case of a pure least squares reconstruction (such as in (9)), the image $\hat{\mathbf{g}}$ reconstructed from the measurements $\mathbf{\eta}$ was found to be the minimizer of

$$\hat{\mathbf{g}} = \arg\min_{\tilde{\mathbf{g}}} ||\mathbf{B}\tilde{\mathbf{g}} - \mathbf{\eta}||^2 \qquad (25)$$

with the SSR corresponding to this solution given by

$$\epsilon = \min_{\tilde{\mathbf{g}}} ||\mathbf{B}\tilde{\mathbf{g}} - \mathbf{\eta}||^2. \qquad (26)$$

TABLE I
RELATIVE RECONSTRUCTION SSR

	NeSh	Normalized Ellipse	Inverse Area Ellipse
No Regularization	1	1.06	0.84
Regularized (low smoothing)	1	0.71	0.68
Regularized (high smoothing)	1	1.08	0.87

If the projection matrix B perfectly matches the true projection function and the measurements η are noise free, the reconstructed SLF image $\hat{g}$ will exactly match the true SLF and the SSR of the would be 0. In practice, the presence of noise and differences between the theorectical projection model and actual propagation will cause the SSR to increase. However, because our testbed was capable of making measurements with low noise, the primary contributor to the SSR in our reconstruction will be the mismatch between the shadowing model and the radio propagation described by the measurements. This means that we can use the SSR from each of the reconstructions as a proxy to determine how consistent the shadowing model is with the true propagation model.

One important caveat is that in the regularization with regularization what is minimized is not the SSR, but instead the SSR plus a regularization term quantifying how well the solution matches the prior information. This will have the effect of increasing the SSR when the LS reconstruction does not match the prior information. Note that in our case we used the covariance from Eq. (3) as the prior for regularization, so deviations in the LS reconstructed SLF from that of a spatial correlated Gaussian random field (with parameters σ_η^2 and κ) will increase the SSR. Another factor that affects the SSR of the results in the resolution of the reconstructed image. As the resolution of the reconstruction increases there are more degrees of freedom for the reconstruction to match the model to the measurements, reducing the SSR. This reduction in SSR does not imply an improvement in the consistency of the model due to the potential for overfitting. For this reason we will only examine the relative SSR of the shadowing models in the reconstructions for each of the scenarios.

The SSR for the reconstruction for these scenarios is shown in Table I normalized by NeSh model SSR. That is, the table values are $\text{SSR}/\text{SSR}_{\text{NeSh}}$. From the table it is apparent that the Inverse Area Ellipse model has a significantly lower SSR than the other methods regardless of the scenario. This implies a much better match between the Inverse Area Ellipse model and the shadowing environment present during the experiments.

Of course the SSR can only show how well the model matches the underlying shadowing process. Since in RF tomography we are concerned not so much with matching measurements to the model, as would be the case in channel estimation, but instead detecting and tracking objects responsible for shadowing. It is possible, that the model that best matches the underlying shadowing process does not produce the best reconstruction for RF tomography. We examine this aspect of the problem through a visual comparison of the reconstructed images by matching the reconstructed images against the shape of the structure.

Figure 6 shows the reconstructed images for the "No Regularization" scenario. For clarity, we have overlaid a diagram of the actual position of the artificial structure in these images. From the figures, the reconstruction using the NeSh model clearly does not correspond to the test structure. In contrast, both the Normalized Ellipse and Inverse Area Ellipse models show what looks to columns from the 2x4 framing and the stack of cinderblocks. While the columns are visible in the reconstructions of both of these models, they are more distinct Inverse Area Ellipse model reconstruction. Note that, while the NeSh model had a lower SSR than the Normalized Ellipse model for this scenario in Table I, and so could be said to be a better model of the propagation environment, the actual reconstructed image was not useful for RF tomography.

The reconstructed images using regularization from the "low smoothing" scenario, shown in Figure 7 are able to provide a test of the resolution limits of the shadowing models. The NeSh model, shown in Figure 7(a), still does not match the expected state of the structure. In the Normalized Ellipse reconstruction from Figure 7(b), a rough outline of the building can barely be distinguished, despite the noise-like artifacts obscuring the image. The large amount of noise and artifacts in the reconstruction suggest that this shadowing model is not able to support such a high resolution reconstruction. The Inverse Area Ellipse model's reconstruction, shown in Figure 7(c), provides a clearer reconstruction of the structure with significantly fewer artifacts. This shadowing model was able to support a relatively high resolution reconstruction with a much smaller amount of noise and artifacts than the other methods. Note however, even at this resolution, the thin walls are not clearly distinguishable. This is not unexpected due to their thickness being well below the diffraction limit for the signal, but does suggest limitations in the capabilities of RF tomography.

For the "high smoothing" scenario however, the Normalized Ellipse model appears to generate the best tomographic reconstruction despite of having the highest corresponding SSR in Table I. This is shown in Figure 8. The NeSh model is still unable to recover the structure of the object in the shadowing environment. The Inverse Area Ellipse reconstruction recovers the basic shape, but the edges are not nearly as sharp as the Normalized Ellipse reconstruction. This makes sense, because the weights for the Inverse Area Elliptical tomographic projection model are more continuous than those of the Normalized Ellipse model. For this reason, the Inverse Area Elliptical reconstruction does not need the additional smoothing to obtain a useful reconstruction. Further the high SSR associated with the Normalized Ellipse reconstruction suggests the regularization is being heavily relied upon to compensate for artifacts caused by the more binary projection used by the Normalized Ellipse model. While this allows the Normalized Ellipse model to create a useful reconstruction in this specific case, the higher reliance on regularization not only suggests that it may not be as good a shadowing model as the Inverse Area Model, but also makes it vulnerable to mismatch between the regularization prior and whatever is being imaged.
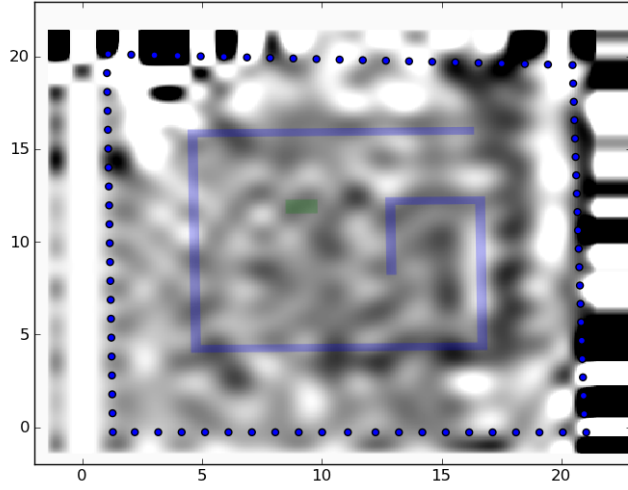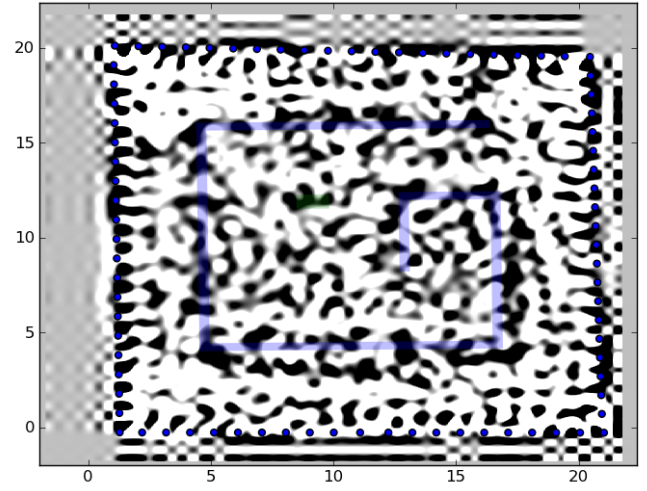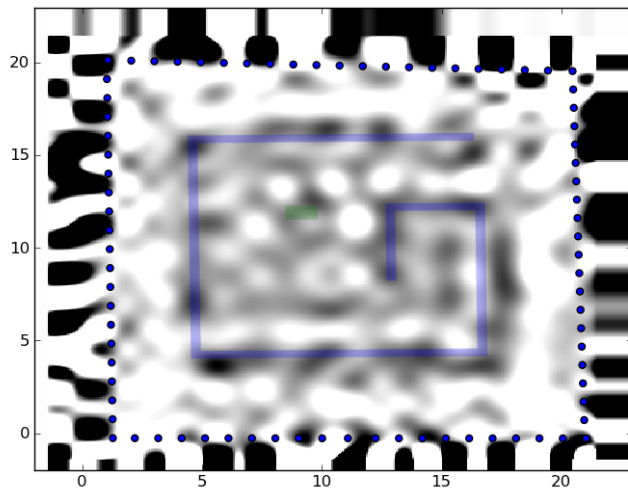
(a) NeSh Model
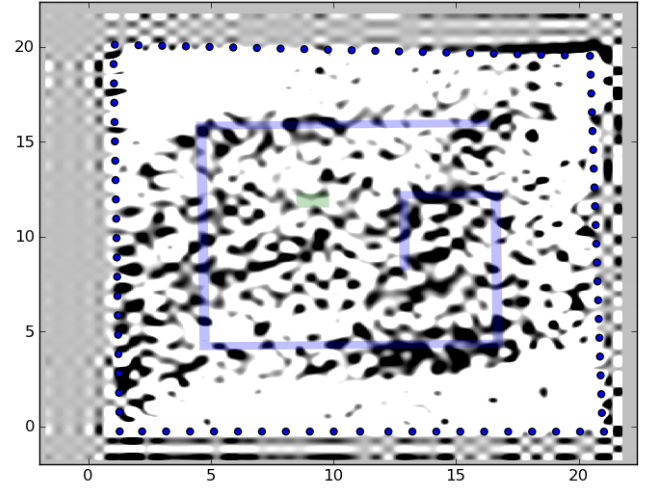
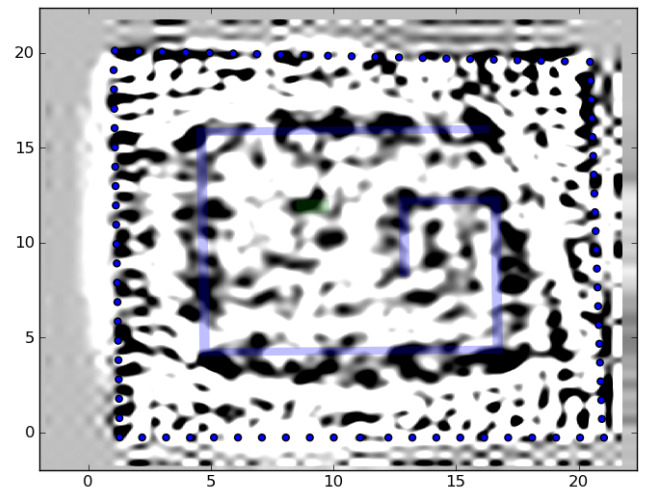(a) NeSh Model
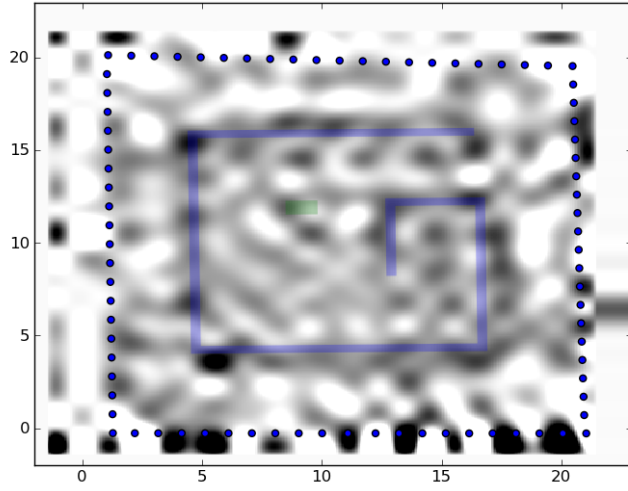
(b) Normalized Ellipse

(b) Normalized Ellipse

(c) Inverse Area Ellipse

(c) Inverse Area Ellipse
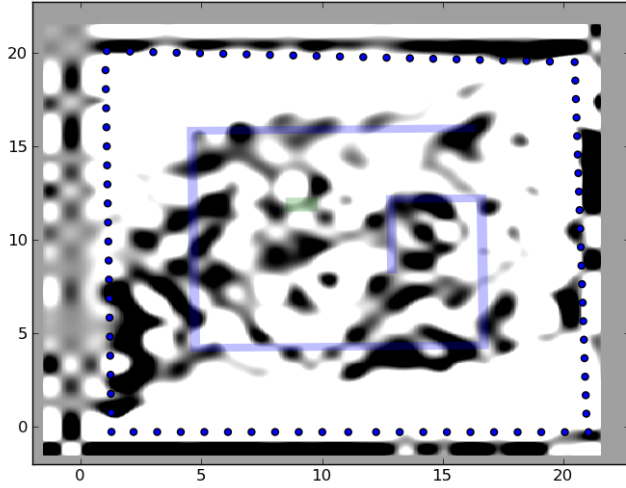
Fig. 6.   Reconstructions, no Regularization

Fig. 7.   Reconstructions, low smoothing

(a) NeSh Model

(b) Normalized Ellipse

(c) Inverse Area Ellipse

Fig. 8.   Reconstructions, high smoothing

V. CONCLUSION

In this paper we examined two existing shadowing models for RF tomography, the NeSH model and Normalized Ellipse model, and presented our Inverse Area Elliptical model. We also described the design of our RF tomography testbed which included a complicated building-like structure and was designed to collect high fidelity signal strength measurements. Measurements collected from a field test using the testbed were then used to analyze both how well the three shadowing models matched the observed radio propagation environment as well as their utility for RF tomography. The results show that RF tomography can be used to image complicated building-like structures, and that the proposed Inverse Area Elliptical model most closely matched the shadowing environment experienced in our field test.

REFERENCES

[1] I. F. Akyildiz, W. Su, Y. Sankarasubramaniam, and E. Cayirci, "Wireless sensor networks: a survey," *Computer Networks*, vol. 38, no. 4, pp. 393 – 422, Mar. 2002.

[2] J. Wilson and N. Patwari, "Radio tomographic imaging with wireless networks," *IEEE Trans. Mobile Comput.*, vol. 9, no. 5, pp. 621–632, 2010.

[3] ——, "See-through walls: Motion tracking using variance-based radio tomography networks," *IEEE Trans. Mobile Comput.*, vol. 10, no. 5, pp. 612–621, 2011.

[4] B. R. Hamilton, X. Ma, R. J. Baxley, and S. M. Matechik, "Radio frequency tomography in mobile networks," in *Proc. IEEE SSP*, 2012, pp. 508–511.

[5] G. T. Herman, *Fundamentals of Computerized Tomography: Image Reconstruction from Projections*, 2nd ed.   Springer, 2009.

[6] M. Youssef, M. Mah, and A. Agrawala, "Challenges: device-free passive localization for wireless environments," in *Proc. ACM MOBICOM*, 2007, pp. 222–229.

[7] L. L. Monte, L. K. Patton, and M. C. Wicks, "Direct-path mitigation for underground imaging in RF tomography," in *Proc. ICEAA*, 2010, pp. 27–30.

[8] M. C. Wicks, "RF tomography with application to ground penetrating radar," in *Proc. ACSSC*, 2007, pp. 2017–2022.

[9] G. L. Stüber, *Principles of Mobile Communications*, 2nd ed.   Kluwer Academic Publishers, 2001.

[10] F. Graziosi and F. Santucci, "A general correlation model for shadow fading in mobile radio systems," *IEEE Commun. Lett.*, vol. 6, no. 3, pp. 102–104, 2002.

[11] M. Gudmundson, "Correlation model for shadow fading in mobile radio systems," *Electronics Letters*, vol. 27, no. 23, pp. 2145–2146, 1991.

[12] P. Agrawal and N. Patwari, "Correlated link shadow fading in multi-hop wireless networks," *IEEE Trans. Wireless Commun.*, vol. 8, no. 8, pp. 4024–4036, Aug. 2009.

[13] N. Patwari and P. Agrawal, "NeSh: A joint shadowing model for links in a multi-hop network," in *Proc. IEEE ICASSP*, 2008, pp. 2873–2876.

[14] Y. Mostofi, "Compressive cooperative sensing and mapping in mobile networks," *IEEE Trans. Mobile Comput.*, vol. 10, no. 12, pp. 1769 – 1784, Dec. 2011.

[15] N. Patwari and J. Wilson, "Spatial models for human motion-induced signal strength variance on static links," *IEEE Trans. Inf. Forensics Security*, vol. 6, no. 3, pp. 791–802, 2011.

[16] C. Liu, D. Fang, Z. Yang, X. Chen, W. Wang, T. Xing, N. An, and L. Cai, "RDL: A novel approach for passive object localization in WSN based on RSSI," in *Proc. IEEE ICC*.   IEEE, 2012, pp. 586–590.

[17] S. Saunders and A. Aragn-Zavala, *Antennas and Propagation for Wireless Communication Systems*.   John Wiley & Sons, May 2007.

[18] J. Wilson and N. Patwari, "Regularization methods for radio tomographic imaging," in *Proc. Virginia Tech Wireless Symposium*, Jun. 2009.

[19] "The universal software radio peripheral (USRP)," Ettus Research LLC. [Online]. Available: http://www.ettus.com/

[20] Z. Yu, R. J. Baxley, B. T. Walkenhorst, and G. T. Zhou, "Channel sounding waveforms design for asynchronous multiuser MIMO systems," *IEEE Trans. Antennas Propag.*, March, 2013 (submitted).

[21] M. E. Brezinski, *Optical Coherence Tomography: Principles and Applications*.   Academic Press, 2006.
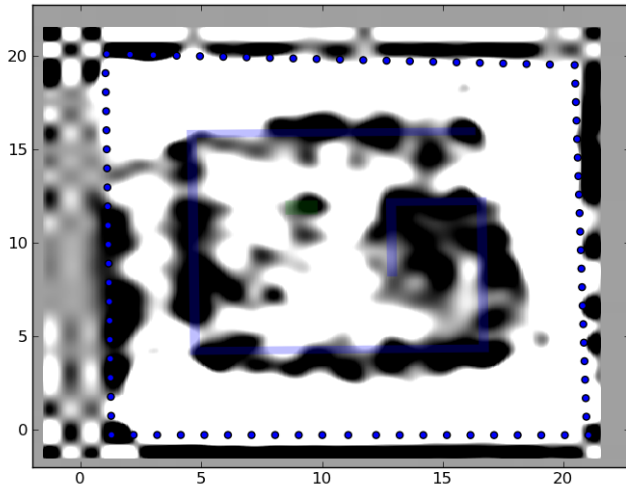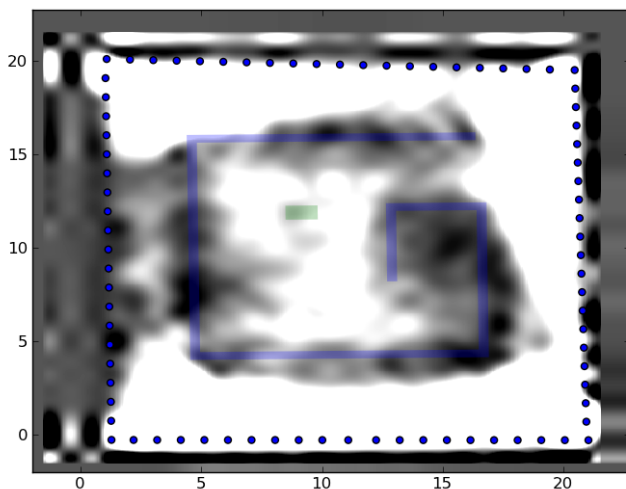
Benjamin "Russ" Hamilton received his B.S. in Electrical Engineering from Auburn University in 2005, his M.S. and Ph.D. in Electrical and Computer Engineering from the Georgia Institute of Technology in 2007 and 2012. Dr. Hamilton was awarded the Georgia Tech Research Institute Shackleford Fellowship in 2009. While at Georgia Tech, he performed research on synchronization and channel estimation in wireless systems and focused on distributed estimation in wireless networks for his dissertation. After receiving his Ph.D., Dr. Hamilton joined the the Communications division of MIT Lincoln Laboratory as a member of the Technical Staff. His research focuses primarily on communications and networking in the airborne tactical domain.

Xiaoli Ma received the B.S. degree in Automatic Control from Tsinghua University, Beijing, China in 1998, the M.Sc. and Ph.D. degrees in Electrical Engineering from the University of Virginia in 2000, and the University of Minnesota in 2003. After receiving her Ph.D., Dr. Ma joined the Department of Electrical and Computer Engineering at Auburn University, where she served as an assistant professor until Dec. 2005. Since Jan. 2006, she has been with the School of Electrical and Computer Engineering at Georgia Tech, where she is currently an Associate Professor. Her research focuses on networking and communications, including transceiver designs for wireless time- and frequency-selective channels, channel estimation and equalization algorithms, carrier frequency synchronization for OFDM systems, localization, performance analysis and cooperative designs for wireless networks. Dr. Ma is a senior member of IEEE, served as an Associate Editor for IEEE Signal Processing Letters (2007-2009) and IEEE Transactions on Wireless Communications (2008-2013), was a member of the Signal Processing Theory and Methods (SPTM), and is a member of Signal Processing for Communications and Networking (SPCOM) Technical Committees of the IEEE Signal Processing Society. She is also an area editor of Elsevier Digital Signal Processing since June 2012.

Robert J. Baxley (SM'13) is a Senior Research Engineer with the Georgia Tech Research Institute (GTRI) Information and Communications Lab, Director of the GTRI Software Defined Radio Lab and an Adjunct Professor in the School of Electrical and Computer Engineering at Georgia Tech. He received the B.S. degree in 2003, the M.S. degree in 2005, and the Ph.D. degree in 2008, all in Electrical Engineering from Georgia Tech. Dr. Baxley currently served as an Associate Editor of DIGITAL SIGNAL PROCESSING. His research interests include communications theory and signal processing.

Stephen M. Matechik (M92) was born in Florida, the United States of America, in 1961. He received the B.S. degree in electrical engineering from the Pennsylvania State University, University Park, Pennsylvania in 1983; and the M.S.E.E. and Ph.D. degrees from the Air Force Institute of Technology (AFIT), Wright-Patterson Air Force Base, Ohio, United States of America, in 1988 and 1996, respectively. In 1983, he was commissioned an officer in the United States Air Force, during which time he was awarded the Air Force Research Laboratory Ralph I . Cole Engineer of the Year Award, and was recognized as Outstanding Engineer of the Year for all Air Force Field Operating Agencies. In 2004 he retired from the Air Force in the grade of Lieutenant Colonel as Technical Director of the Command and Control Battlelab. He joined the MITRE Corporation, a federally funded research and development corporation, and as a Principal Information Systems Engineer and Principal Investigator, received several research and mission partner awards, to include an award from the MITRE Senior Vice-President and General Manager for Kaleidoscope, an advanced content-based video indexing and retrieval capability for unmanned aerial vehicle (UAV) exploitation cells. Early in 2010, he was hired as Principal Research Faculty to the Information and Communications Laboratory of Georgia Tech Research Institute, Atlanta, Georgia, United States of America, where his current research interests include video informatics, analytics, and taxonomies; radio tomographic imaging; multi-sensor fusion; and unmanned and autonomous systems. Dr. Matechik is a member the Armed Forces Communications and Electronics Association (AFCEA), and the Association for Unmanned Vehicle Systems International (AVUSI). He is also a member of the IEEE Signal Processing Society.